The International Archives of the Photogrammetry, Remote Sensing and Spatial Information Sciences, Volume XLVIII-2/W7-2024
Optical 3D Metrology (O3DM), 12–13 December 2024, Brescia, Italy

Modeling the uncertainty of indirect calculations from 2D detected edges of projected 3D circular markers' centers in photogrammetric systems

Oier Saez de Egilaz[1,*], Iñigo Auzmendi Iriarte[1] , Pedro González de Alaiza Martínez[1] and Ibai Leizea[1]

[1] IDEKO, Basque Research and Technology Alliance (BRTA), 20870 Elgoibar, Spain
Technical Commission II

Keywords: Eccentricity Error, Pinhole Projection, Projection Anisotropy, Optical Circular Markers, Uncertainty Modeling.

Abstract

Optical markers' centres' calculation, indirectly inferred from fitted ellipses' borders, is subject to uncertainties which arise from both noise in data and systematic errors and whose nonlinear propagation has a strong impact on the attainable overall uncertainty of industrial close-range photogrammetric systems. Based on both exhaustive experimental measurements and a revisit of pinhole projection theory mapping the 2D detected ellipses' borders onto 3D circular markers' borders, the detection's precision, shown to be independent of systematic errors and markers' size in the range of sizes 40-160 px, is characterized as a function of markers' gray intensity and orientation, both of which measurable during image processing. The proposed model has two or three experimental coefficients which need to be customized according to the used camera-lens system and edge-detection algorithm.

1. Introduction

Manufacturing of large parts (Mendikute et al., 2017) and high-precision robot guidance and calibration (Zakeri and Xie, 2024) are examples of industrial applications which nowadays necessitate the assistance of external high-accuracy metrological tools, such as CMM's (Lavecchia et al., 2018) or Laser-Trackers (Filion et al., 2018), to fulfill the demanding accuracy requirements of the market. Industrial close-range photogrammetry with optical markers has the potential for competing against these at higher versatility and significantly lower cost. Nevertheless, reaching unquestionably an overall accuracy below 0.1 mm in the meter range (Gharaaty et al., 2018), immediately appealing to this industrial context, is conditioned by the nonlinear propagation of numerous uncertainty sources of both systematic (accuracy) and random (precision) nature (Sims-Waterhouse et al., 2020). Modeling them realistically as a function of scene's variables, what would allow their effective compensation and control, still remains an open problem. On the one hand, precision, inherent to processing of noisy image data, is typically modeled by Gaussian distributions of assumed or barely estimated standard deviations, what may indeed predict the total precision of the photogrammetric system, but rather qualitatively than quantitatively. On the other hand, the dramatic impact that systematic errors have upon the quality of the photogrammetric measurement is well known, but, in practice, due to their intricacy, most of the time they are ignored, not fully compensated, or incorrectly treated also as random variables of greater standard deviation than the noise itself existing in data, what seriously compromises the reliability of the photogrammetric tool. In effect, not correcting them one by one —trying to filter them by redundancy of acquired data is useless (Luhmann, 2014a)— is translated into photogrammetric measurements more discrepant than expected. In this sense, the uncertainty of markers' centres' detection, which has the greatest effect on the photogrammetric system's final behavior, has been a topic of active research for more than five decades, because both systematic and random error components coexist and, unfortunately, actions on mitigating one aggravate collaterally the other.

One of the most common methods for detecting the centers of circular optical markers relies on edge detection (Luhmann et al., 2020, Chapter 5.4.2.5). The total uncertainty of this calculation stems from the determination of edges by image processing and the inference of centers from edges by solving the perspective. On the one hand, the former uncertainty depends primarily on the edge-detection algorithm employed to determine raw edges' points (distorted), the camera's intrinsic parameters' calibration used to undistort them, and the criterion to fit an ellipse to the undistorted edges' points. Incidentally, the raw edges' points' detection may be affected, in turn, by, among others, the markers' relative size, orientation and illumination degree, as well camera's sensor's noise calibration. In this regard, the precision of this calculation as a function of markers' size has been studied in depth since early 80's, from first theoretical models (Förstner, 1984) to subsequent validations by simulations (Trinder, 1989) and experiments (Shortis et al., 1995, Dauvin et al., 2018), concluding that the bigger the marker, the more precise its detection, independently of the noise level present in images and the bit depth. On the other hand, the uncertainty of inferring the markers' centers is above all influenced by eccentricity errors (systematic) —differences between the projected centers and the centers of the corresponding fitted ellipses caused by non-affine essence of the pinhole projection (Wrobel, 2012)—, especially when seen markers' sizes exceed 10 pixels (Luhmann et al., 2020, Chapter 3.6.1.2). Precisely, to a tolerable detriment of precision, the compromise solution of working with sizes of 5-10 px and neglecting eccentricity errors has been widely used (Robson et al., 2018, Pottler et al., 2005), even if, by doing so, achieving high accuracy may be compromised (Luhmann, 2014b). Notwithstanding, this solution may not be viable in complex scenes where the working-distance range is broad and/or planning a distribution of optical markers of different size within the scene is not feasible, such as in multi-camera applications and robot tracking. Furthermore, shrinking the seen markers' sizes reduces the amount of information available for discerning the edges themselves and the 3D geometrical properties that can be computed from them (Otepka and Fraser, 2004), what does not reduce the net uncertainty of the detection (Mordwinzew et al., 2015).

* Correspondence: osaezdeegilaz@ideko.es; Tel.: +34-943-748-000

The objective of this work is to model realistically the precision of marker's centers' detection for the particular case of optical circular markers which are completely seen as eccentric ellipses of size of several tens of pixels. The proposed model is based on both exhaustive experimental measurements and a revisit of the pinhole projection theory mapping the 2D detected borders of ellipses onto 3D circular markers' borders. This paper is organized as follows. In Section 2 the experimental setup is described, the eccentricity-error correction is revisited, and the image-processing algorithm is detailed. In Section 3 the statistical analysis of results is performed, and the model is derived and discussed. Finally, in Appendix there are important formulae concerning the pinhole projection and ellipse's representation used throughout the paper.

2. Materials and methods

2.1 Experimental set-up

Figure 1. Experimental set-up: granite table, camera-lens system, light source, optical circular retroreflective markers (hemispheres) and support structures.

Figure 1 shows the photogrammetric measuring set-up designed to characterize the marker-detection precision. It consists of a measuring device (camera-lens system plus illumination device) and sixteen optical markers, which are all firmly attached onto a granite table. On the one hand, the industrial camera used is a Teledyne Dalsa Genie Nano M2590, which has a resolution of 2592×2048 pixels (5.3 MP) and a pixel size of 4.8×4.8 µm. The lens is a Schneider Optics Kreuznach Cinegon, with a F-number of 1.8 mm and a fixed focal length of 16 mm. The ring-shape light source is a DCM ALB0810A-W00i/AN, which is physically separated from the camera-lens system. On the other hand, each marker is composed of a 1.5-inch-diameter steel hemisphere with a 20-mm-diameter circular non-coded retroreflective optical target, a Hubbs Metrology Solutions SBR-1.500-20MM, mounted on a 1.5-inch-diameter magnetic ball probe seat monument, and a Metrologyworks BT-A-Y-BPSM-Y. These present the advantages of being orientation-adjustable without altering the location of their 3D centers, what is used as ground truth for eccentricity error, and of being precisely measurable by a Laser Tracker, in this paper concretely by an Hexagon Leica Absolute Tracker AT960. The markers are randomly distributed onto the granite table, at distances between 335 and 1260 mm from the camera, such that, as shown in Fig. 2, the image plane be as filled as possible despite the geometrical limitations. They appear in images with sizes ranging from 40 to 160 pixels.

The goal of the experiment is to characterize the markers' detection precision as a function of scene variables such as markers' position and orientation and illumination degree. To create a database for this purpose, four layouts (a random reorientation of markers plus a change in exposure time and/or light source's position) were photographed a statistically significant number of times in order to compute the standard deviation of each marker's center's detection. Relative motion among makers and/or camera-lens system must be mitigated as much as possible, not to attribute deviations of camera's extrinsic parameters and/or markers' positions to the detection itself. In this sense, first, a granite table was chosen because this material offers a low thermal expansion and high rigidity. Additionally, it was endowed with a pneumatic suspension in its base, working as a low-pass filter with a cutoff frequency of 15 Hz, to dampen eventual high-frequency vibrations caused by other machines in the laboratory. Second, the experiment was conducted in a dedicated laboratory with climate control, where the temperature is maintained around 20ºC $\pm$ 1ºC. Furthermore, the temperatures of camera's body, lens, illumination, support structures and table were monitored via thermocouples, as shown in Fig. 3, and the internal camera's sensor's temperature via software. A 2-hours-long camera warm-up procedure was carried out prior to measurements (cf. Fig. 4a) to guarantee that all experiments were done in the same steady-state temperature conditions (cf. Fig. 4b), avoiding any measurement disturbance related to dilation (Dauvin et al., 2018). Finally, the data capture was performed at the highest frequency allowed by the camera in experiment's conditions (40 Hz) over a short period of time (90 s). Detection's standard deviations were thus calculated over 3600 photographs.

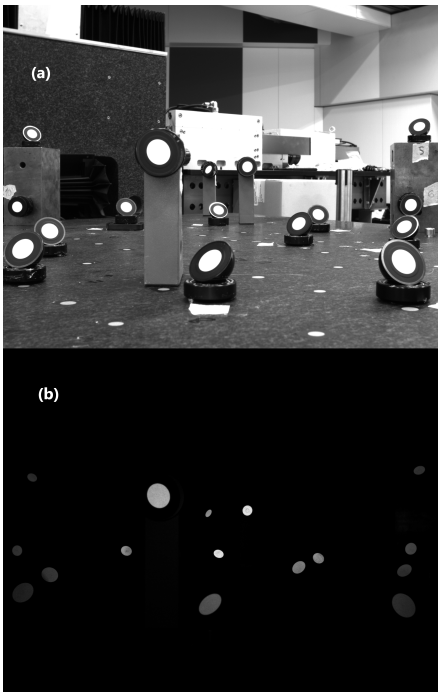

Figure 2. (a) The sixteen markers seen by the camera (image plane) using an exposure time longer than in experiments. (b) Example of image taken under experiment's conditions.

2.2 Mapping 2D ellipses' borders onto 3D circular markers

Let the axes u, v and w be the camera's reference frame, such that axis w be normal to the image plane, $u = v = 0$ be at the center of the image, and the camera be at $w = 0$ following the pinhole model. In this frame, as illustrated in Fig. 5, a

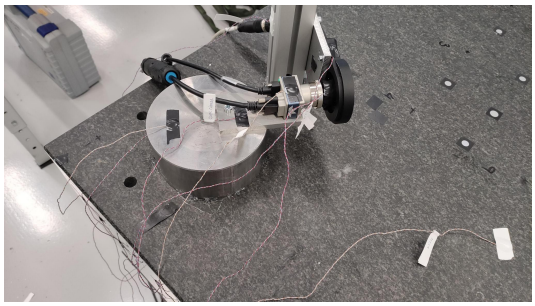

Figure 3. Camera sensor temperature monitoring

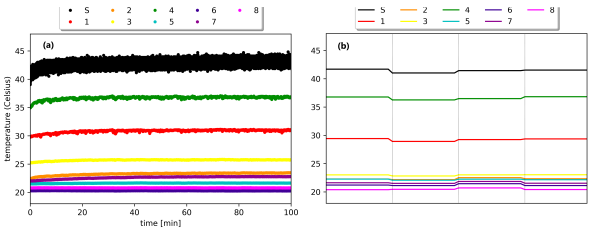

Figure 4. Monitoring: temperatures by thermocouples in colors and internal camera's sensor's temperature by software in black. (a) Temperatures as a function of time during warm-up. (b) Temperatures over time of the four experiments done.

3D circular marker can be unambiguously defined by its center $(u_c, v_c, w_c)^T$, its radius r, and a normal unit vector to its plane. For instance, without loss of generality, we shall define this unit normal vector as $\hat{\boldsymbol{n}}_\perp = (\cos\theta\cos\phi, \cos\theta\sin\phi, \sin\theta)^T$, where the angles θ and ϕ represent the latitude and the longitude, respectively, with θ chosen such that the w-component of $\hat{\boldsymbol{n}}_\perp$ be non negative.

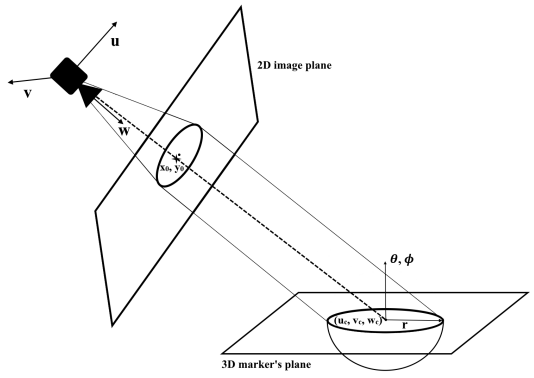

Figure 5. Pinhole camera-model marker-projection representation: the border of a 3D circular marker is seen as a 2D ellipse on image plane.

The following unit vector is perpendicular to $\hat{\boldsymbol{n}}_\perp$ and hence lies on the plane of the circle:

$$\hat{\boldsymbol{n}}_\parallel = (\sin\theta, 0, -\cos\theta\cos\phi)^T / \sqrt{1-\cos^2\theta\sin^2\phi}. \quad (1)$$

Points at the border of the 3D circular marker, $(u, v, w)^T$, can be calculated by rotating $r\hat{\boldsymbol{n}}_\parallel$ around the axis defined by $\hat{\boldsymbol{n}}_\perp$ through all angles α:

$$(u, v, w)^T = (u_c, v_c, w_c)^T + \bar{\bar{R}}_\alpha r\hat{\boldsymbol{n}}_\parallel, \quad (2)$$

where $\bar{\bar{R}}_\alpha$ is the necessary rotation matrix, which can be computed via Rodrigues' rotation formula:

$$\bar{\bar{R}}_\alpha = \bar{\bar{I}} + \sin\alpha\bar{\bar{S}} + (1-\cos\alpha)\bar{\bar{S}}^2, \quad (3)$$

$$\bar{\bar{S}} = \begin{pmatrix} 0 & -\sin\theta & \cos\theta\sin\phi \\ \sin\theta & 0 & -\cos\theta\cos\phi \\ -\cos\theta\sin\phi & \cos\theta\cos\phi & 0 \end{pmatrix}. \quad (4)$$

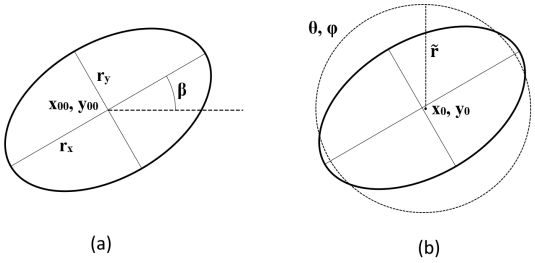

Figure 6. Two equivalent parametric descriptions of the 2D ellipse. (a) 2D point of view: canonical parameters. (b) 3D point of view: Kager's parameters.

Under the pinhole model and assuming no distortion caused by the lens, the 3D border in Eq. (2) is projected on the image plane as the 2D border $(x, y)^T = (u/w, v/w)^T$, working with dimensionless pixel coordinates. This 2D border is an ellipse and, after some manipulations, it satisfies the following quadratic equation:

$$a + bx + cx^2 + dxy + ey + fy^2 = 0, \quad (5)$$

where the expressions for these six coefficients are given in Appendix. This 2D ellipse has five degrees of freedom, since its equation is homogeneous. From 2D point of view, it can be described by the canonical parameters (cf. Fig. 6a): its center $(x_{00}, y_{00})^T$, its radii r_x and r_y, and its rotation angle β. Alternatively, from 3D point of view, it can be defined by the following five parameters related to the above-mentioned ones of the 3D circular marker (cf. Fig. 6b): its projected center $(x_0, y_0)^T = (u_c/w_c, v_c/w_c)^T$, its orientation angles θ and ϕ, and its relative radius $\tilde{r} = r/w_c$.

The difference between $(x_0, y_0)^T$ and $(x_{00}, y_{00})^T$ is known as *eccentricity error* (Luhmann, 2014b). Knowing that $x_{00} = (2fb - de)/(d^2 - 4cf)$ and $y_{00} = (2ce - db)/(d^2 - 4cf)$ and taking account of the expression for the quadratic coefficients given in Appendix, after some manipulations, this error is calculated:

$$x_0 - x_{00} = -\tilde{r}^2\cos\theta(x_{00}\cos\theta + \sin\theta\cos\phi), \quad (6)$$

$$y_0 - y_{00} = -\tilde{r}^2\cos\theta(y_{00}\cos\theta + \sin\theta\sin\phi), \quad (7)$$

which is zero only if $\theta = \pi/2$, i.e., if the plane of the 3D circular marker is parallel to the image plane. In the same way, the ellipse's radii and the rotation angle could be computed, as explained in Appendix. Interestingly, the product of radii verifies:

$$\frac{r_x^2 r_y^2}{\tilde{r}^4} = \frac{(\sin\theta + x_0\cos\theta\cos\phi + y_0\cos\theta\sin\phi)^2}{(1-\tilde{r}^2\cos^2\theta)^3}, \quad (8)$$

which means that, when $\theta = \pi/2$, the 3D marker would be seen as a circle of radius $\tilde{r}$, as illustrated in Fig. 6b.

Due to the loss of information caused by the pinhole projection, the map of the 2D ellipse's border onto the 3D circular marker's border is not bijective. Indeed, Helmut Kager demonstrated that for each description of the 2D elliptic border there are two distinct possible descriptions of the 3D marker (Kager, 1981). We shall follow his work, based on relating invariant values of the ellipse (obtained from eigen-decomposition) to a unitary cone, to compute the two distinct possible values for x_0, y_0, θ and ϕ. Incidentally, the calculation of the fifth parameter $\tilde{r}$ is missing in his work. However, once the other four are known, it can be easily calculated using two coefficients of the ellipse's equation. For instance:

$$\tilde{r} = \sqrt{\frac{F_2 c - C_2 f}{C_1 f - F_1 c}}, \tag{9}$$

where the expressions for C_1, C_2, F_1 and F_2 are detailed in Appendix.

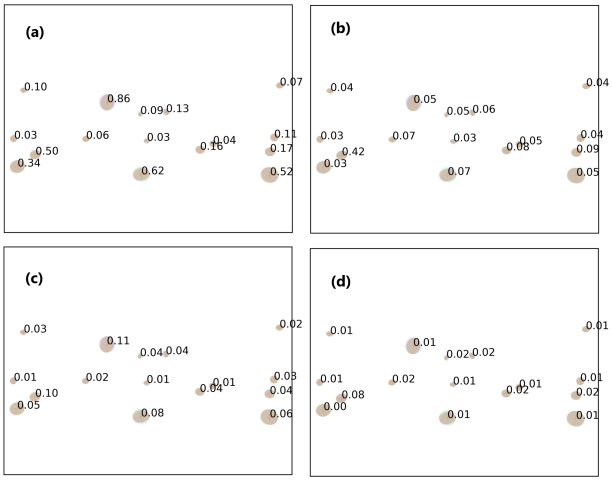

Figure 7. Discrepancy among four random orientations superimposed of each hemisphere. (a,c) Discrepancy among ellipses' centers in pixels and mm, respectively. (b,d) Discrepancy among Kager's selected centers in pixels and mm, respectively. Discrepancy in mm reduces by an order of magnitude when correcting the eccentricity error.

Selecting the correct solution from the two Kager's candidates calculated from the 2D detected border, which is subject to uncertainty, is a complex task (Ahn and Kotowski, 1997). In this paper, the choice is made by the criterion of lowest discrepancy among multiple images, taken with fixed extrinsic parameters, of the hemisphere at different orientations, since its 3D center is invariant under rotation by construction. The effectiveness of this criterion to correct the eccentricity error in this experiment is illustrated by Fig. 7, which superimposes four random layouts measured consecutively (cf. Fig. 2). Effectively, in pixels, the discrepancy in Kager's centers, $\max_{i,j} ||(x_0, y_0)_i - (x_0, y_0)_j||$ with i and j referring to layouts (Fig. 7a), is smaller than in ellipses' centers, $\max_{i,j} ||(x_{00}, y_{00})_i - (x_{00}, y_{00})_j||$ (Fig. 7b). This reduction is more remarkable, of an order of magnitude, when translating them into mm (cf. Fig. 7c and 7d).

2.3 Edge-Detection algorithm

Image processing for detecting markers' edges' points is carried out in two stages. First, Canny edge-detector algorithm is applied to naïvely detect candidates for markers' contours (Canny, 1986). It is used both as a filter, discarding non-elliptical candidates (false positives), and as seed for the subsequent stage. Second, a subpixel-level correction is applied to the retained detected borders' points. Several subpixel-level algorithms exist in the bibliography, such as Zernike Moments (Ghosal and Mehrotra, 1993), Partial Area Effect (Trujillo-Pino et al., 2013) and Gaussian Fitting (Wang et al., 2022). Nevertheless, in this paper, since the focus is solely on precision, a simpler method based on image interpolation is employed because it is algorithmically more robust, with no adjustable parameter but an up-scaling factor, even if it is computationally less efficient. For each valid marker's contour an axis-aligned crop that fully contains the ellipse is made and enlarged using linear interpolation. In this research an up-scaling factor of 64 is used since convergence tests showed stabilization beyond 32. In the resulting enlarged image, Otsu binarization is performed (Otsu, 1979), followed by contour detection (Suzuki and Abe, 1985). Finally, the detected contour is transformed back to the original image's position and size. Next, the subpixel-level markers' contours obtained from this image-interpolation method are undistorted thanks to Brown model (Brown, 1971). The corresponding intrinsic parameters were calibrated at the beginning of the experiments following the procedure in (Leizea et al., 2023). Finally, the elliptical equation given by Eq. (5) is fitted to these undistorted edges's points (Fitzgibbon and Fisher, 1995). Markers' centers are inferred from the resulting ellipses as above explained in Sec. 2.2.

3. Experimental results and discussion

3.1 Experimental results

A comprehensive database containing 64 instances of marker detection (4 layouts of 16 markers each) was created from experiments. There, the precision of each detection, calculated as the standard deviations, over 3600 images, of ellipse's degrees of freedom (in particular, $\sigma_{x_{00}}$ and $\sigma_{y_{00}}$ from the canonical 2D-point-of-view description, and σ_{x_0}, σ_{y_0}, σ_θ, σ_ϕ and $\sigma_{\tilde{r}}$ from the Kager's 3D-point-of-view description), is related to all the variables, directly measurable on the image during its processing, related to marker's size and orientation (given by ellipse's parameter sets: $x_{00}, y_{00}, r_x, r_y, \beta$ and $x_0, y_0, \theta, \phi, \tilde{r}$) and marker's degree of illumination. The latter is directly calculated as the average gray intensity of the pixels inside detected contours, I_{gray}, expressed in 8-bit scale from 0 to 255, instead of as a color contrast because the background color distribution is quite uniform and of intensity below 5 (cf. Fig. 2b). In the subsequent data analyses outliers are not systematically filtered to avoid data overfitting, prioritizing the robustness of the model (i.e., as less parameters as possible).

Two pairwise correlation-coefficient analyses were performed in the database. Firstly, the Pearson's correlation-coefficient analysis (Pearson, 1895), which highlights linear relationships between variables. Secondly, the Spearman's rank-correlation-coefficient analysis (Spearman, 1904), which, instead, accentuates monotonic relationships. These results are merged into Fig. 8.

On the one hand, Pearson's analysis reveals strong linear correlations among the standard deviations of centers' coordinates, namely, $\sigma_{x_{00}}$ and σ_{x_0}, and $\sigma_{y_{00}}$ and σ_{y_0}. In effect, as shown in Fig. 9 for x dimension, the precision of calculating a marker's center is independent of the inference criterion from detected borders (ellipse's or Kager's center):

$$\sigma_{x_{00}} \approx \sigma_{x_0}, \tag{10}$$

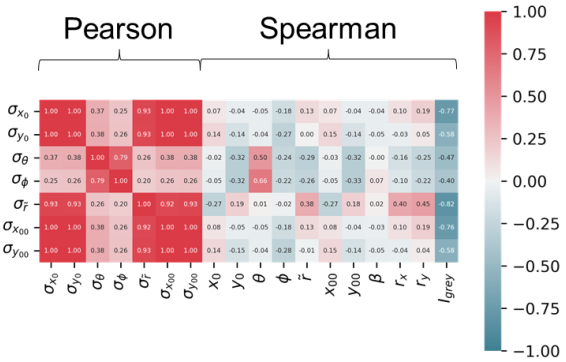

Figure 8. Summary of correlation-coefficient analyses in database.

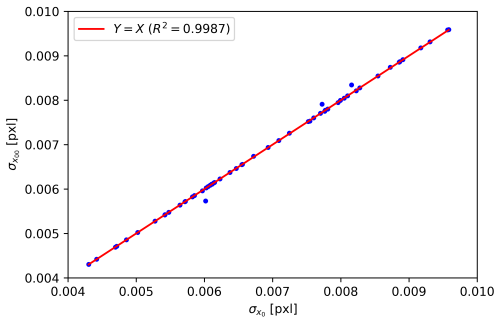

Figure 9. Correlation between $\sigma_{x_{00}}$ and σ_{x_0}.

$$\sigma_{y_{00}} \approx \sigma_{y_0}. \tag{11}$$

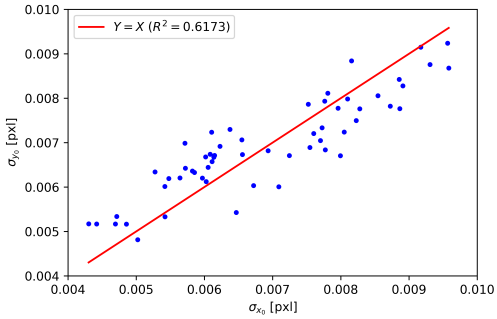

Figure 10. Correlation between σ_{x_0} and σ_{y_0}.

Figure 10 discloses an anisotropy between image plane's x and y axes:

$$\sigma_{x_0} \neq \sigma_{y_0}, \tag{12}$$

even if the calibration of camera-lens system's intrinsic parameters performed prior to experiments yielded a square pixel size. It is greater for more eccentric orientations and ultimately explained by the non-affinity of the pinhole projection.

On the other hand, Spearman's analysis shows strong correlations of the standard deviations of the five Kager's degrees of freedom only with the illumination degree (gray intensity), but not with seen markers' size and orientation. In particular, the strongest correlation concerns the standard deviation of the relative radius, plotted in Fig. 11. It can be modelled by the following power law on the gray intensity:

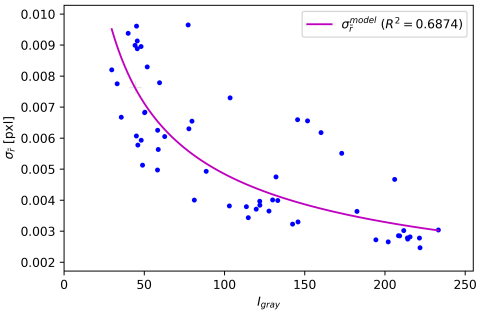

Figure 11. Correlation between I_{gray} and $\sigma_{\tilde{r}}$.

$$\sigma_{\tilde{r}}^{\text{model}} = k_0 I_{\text{gray}}^{k_1}, \tag{13}$$

where $k_0 = 0.0629$ px and $k_1 = -0.5567$ are two experimental coefficients. These may depend on camera's acquisition parameters' calibration (how pixels' color is resolved according to the illumination degree) and on edge-detection algorithm (how the location of ellipses' border is determined according to pixel-color distribution).

3.2 Modelling detection's precision

Pearson's and Spearman's analyses show strong correlations of the standard deviations of center's coordinates, σ_{x_0} and σ_{y_0}, with the standard deviation of the relative radius, $\sigma_{\tilde{r}}$, and the illumination degree, I_{gray}. The latter is conjectured here to be a consequence of the former, and the following Ansatz for markers' centers' detection precision is hence proposed:

$$\sigma_{x_{00},y_{00}}^{\text{model}} = \sigma_{x_0,y_0}^{\text{model}} = C_{x,y}\, \sigma_{\tilde{r}}^{\text{model}}, \tag{14}$$

where the coefficients C_x and C_y, which may be different from each other to account for the projection anisotropy, are calculated by fitting the Ansatz to experimental results with additional assumptions. Interestingly, they are expected to be greater than 1 only if a true subpixel-level correction is applied to edges, where distances like the relative radius $\tilde{r}$ can be determined from detected points with a better precision than single points like (x_0, y_0).

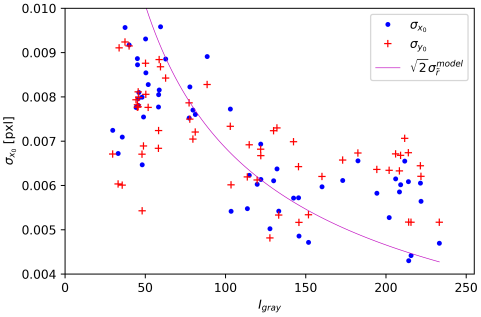

Figure 12. Experimental results vs model 1.

The first assumption that can be done is to make the coefficients C_x and C_y in Ansatz (14) be equal and constant. The simplest model is so obtained, which is compared against experimental

results in Fig. 12, concretely with $C_x = C_y = \sqrt{2}$ in round numbers. It is numerically robust but only gives a rough approximation of the detection precision (error up to $\pm 38\%$ for 85% of data), entirely ignoring the anisotropy.

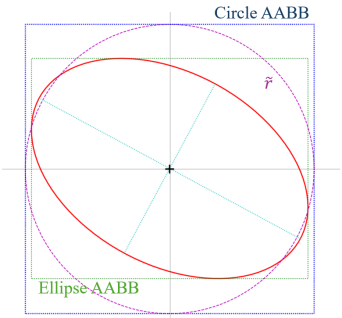

Figure 13. Scale deformation caused by pinhole projection: AABB bounding box of the ellipse (green) vs AABB bounding box of circle of radius $\tilde{r}$ which would be projection of the 3D marker if adjusted parallel to the image plane (blue).

The detection's anisotropy observed experimentally stems from the unequal scale deformation caused by pinhole projection along x and y axes. In this paper it is proposed to calculate geometrically the deformation scale factors by comparing, along each axis, the size of the detected elliptical marker's border with the size of the non-eccentric projection of such marker, i.e., a circle of radius $\tilde{r}$ centerd at (x_0, y_0), as the 3D marker would be seen if it were virtually reoriented parallel to image plane without modifying its 3D center. These sizes can be measured, as depicted in Fig. 13, from axis-aligned bounding boxes (AABB), because they are precisely tangential to borders along the axes in question (cf. Appendix). The marker's border's projection's AABB would go so from a square of side $2\tilde{r}$ to a rectangle of size $L_x^{\text{BBOX}} \times L_y^{\text{BBOX}}$ under the action of pinhole projection. The ratios between their sides can thus be understood as a reliable average estimation of the sought deformation scale factors (the square root is added because the subject of study are standard deviations instead of variances):

$$\varkappa_{x,y} = \sqrt{\frac{L_{x,y}^{\text{BBOX}}}{\tilde{r}}}, \tag{15}$$

which, incidentally, are equal to $\sqrt{2}$ when the marker is parallel to image plane.

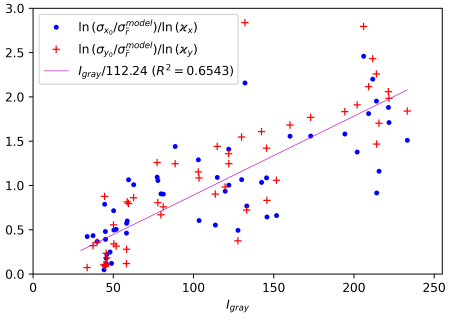

Figure 14. Fitting the degree of freedom k_2 of model 3.

To model the detection's anisotropy, the assumption that the coefficients C_x and C_y in Ansatz (14) are related the corresponding deformation scale factors given by Eq. (15) is made.

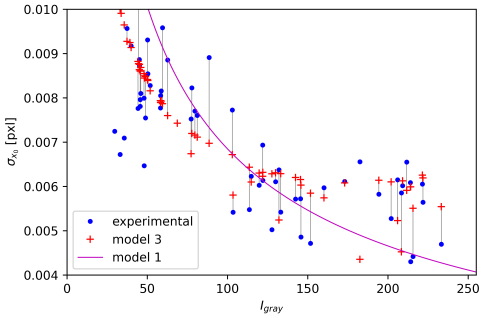

Figure 15. σ_{x_0}: models vs experimental data.

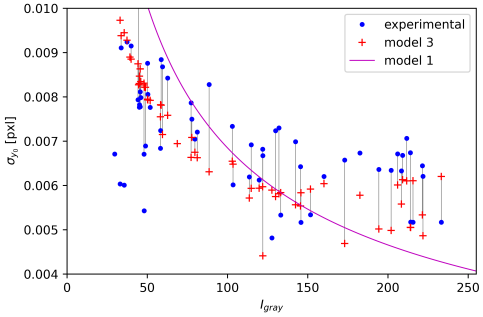

Figure 16. σ_{y_0}: models vs experimental data.

The simplest choice in this sense is $C_{x,y} = \varkappa_{x,y}$. This second model, nevertheless, is not advantageous over the first one, yielding similar error results at a higher computational cost. This is because in the computation of the deformation scale factors the uncertainty of the edge-detection algorithm, which depends on the illumination degree, should be considered. An exponential correction on the illumination degree is introduced in the third proposed model:

$$C_{x,y} = \varkappa_{x,y}^{I_{\text{gray}}/k_2}, \tag{16}$$

where $k_2 = 112.24$ after fitting to experimental data (cf. Fig. 14). Interestingly, for middle gray intensities, around k_2, the exponent becomes unitary and the previous models are recovered. With a third parameter, this model achieves a better goodness of fit, with an error up to $\pm 25\%$ for 85% of data. Figures 15 and 16 compare it with the first one for σ_{x_0} and σ_{y_0}, respectively.

3.3 Discussion

The experiment has shown that, for the chosen industrial camera-lens system and edge-detection algorithm, the detection's precision is of order of 0.01 px, a value in line with previous predictions (Trinder, 1989, Dauvin et al., 2018). This random error component of the uncertainty is independent of systematic ones such as eccentricity errors, distortion-correction errors (calibration of intrinsic parameters) and edge-detection errors (image-processing algorithm), but in this paper only the independence of the first one has been empirically demonstrated. Unlike in previous research works, the primary variable to model the precision of detecting a marker is its illumination degree, quantifiable as its averaged gray intensity during image processing. The better illuminated, the more precise, almost regardless its relative size and orientation, at least for the studied range of sizes (40 to 160 px). This does not necessarily disagree with previ-

ous models, dedicated to smaller sizes, where the improvement in precision with the size predicted there tended to stagnate beyond 16 px notably for gray-color depths above 4 bits (Förstner, 1984, Trinder, 1989). Therefore, the model 1 proposed here, a power law on it with only two experimental coefficients depending on the camera-lens system and the edge-detection algorithm, seems, in its current form, to be robust and realistic enough to already predict, quantitatively rather than qualitatively, the output precision of photogrammetric systems using circular optical markers, for instance, via analytical uncertainty-propagation models or Monte-Carlo simulations, especially in industrial applications where illumination is not guaranteed to be homogeneous, of course, provided that systematic errors be under control. Nevertheless, markers' orientation does also have an impact on the precision (projection anisotropy), minor compared to illumination's, but not completely negligible. In this sense, model 3, which accounts for it, seems to improve the results of model 1 in relative terms, but not in a conclusive way.

4. Conclusions

The uncertainty of industrial close-range photogrammetric measurements crucially depends upon the uncertainty of optical markers' centers' indirect detection. Their inference from detected markers' edges is subject to errors with systematic (accuracy) and random (precision) components. This work presents a comprehensive model of the latter component which is input only by magnitudes measurable during image processing. It is shown that, for marker sizes of several tens of pixels, the detection precision is independent of systematic errors and hinges mainly on markers' gray intensity (accounting for illumination degree) and, to some extent, also on markers' orientation (taking account of anisotropy caused by pinhole projection), but not on their size. The robustness of the model has been prioritized and versions of it with only two and three experimental parameters are presented. It is expected that these adjustable parameters will be able to be extrapolated to other industrial camera-lens systems and edge-detection algorithms, but further research is needed in this regard. The presented precision model can be directly used as input for either analytical uncertainty-propagation models or Monte-Carlo calculations an paves the way for performing more realistic simulations of current industrial photogrammetric systems.

Appendix

The 3D border of Eq. (2) projected onto the image plane can be written as:

$$x = \frac{x_0 + \tilde{r}(a_u \cos\alpha + b_u \sin\alpha)/\sqrt{1-\cos^2\theta\sin^2\phi}}{1 + \tilde{r}(a_w \cos\alpha + b_w \sin\alpha)/\sqrt{1-\cos^2\theta\sin^2\phi}}, \quad (17)$$

$$y = \frac{y_0 + \tilde{r}(b_v \sin\alpha)/\sqrt{1-\cos^2\theta\sin^2\phi}}{1 + \tilde{r}(a_w \cos\alpha + b_w \sin\alpha)/\sqrt{1-\cos^2\theta\sin^2\phi}}, \quad (18)$$

where:

$$a_u = \sin\theta, \quad (19)$$

$$b_u = -\cos^2\theta\cos\phi\sin\phi, \quad (20)$$

$$b_v = \cos^2\theta\cos^2\phi + \sin^2\theta, \quad (21)$$

$$a_w = -\cos\theta\cos\phi, \quad (22)$$

$$b_w = -\cos\theta\sin\theta\sin\phi. \quad (23)$$

Equations (17) and (18) satisfy the quadratic form of Eq. (5), once the parameter α is eliminated through trigonometric manipulations. The six coefficients of the quadratic form are all of the form $q = Q_0 + \tilde{r}^{-2}Q_2 = Q_0 + 2\tilde{r}^{-2}\tilde{Q}_2(1-\cos^2\theta\sin^2\phi)$ for $q = a, b, c, d, e, f$:

$$A_1 = -a_u^2 b_v^2, \quad (24)$$

$$\tilde{A}_2 = \frac{b_v^2}{2}x_0^2 - b_u b_v x_0 y_0 + \frac{c_u^2}{2}y_0^2, \quad (25)$$

$$B_1 = 2a_u a_w b_v^2, \quad (26)$$

$$\tilde{B}_2 = b_v b_w x_0 y_0 - (a_u a_w + b_u b_w)y_0^2 - b_v^2 x_0 + b_u b_v y_0, \quad (27)$$

$$C_1 = -a_w^2 b_v^2, \quad (28)$$

$$\tilde{C}_2 = \frac{c_w^2}{2}y_0^2 - b_v b_w y_0 + \frac{b_v^2}{2}, \quad (29)$$

$$D_1 = 2a_w^2 b_u b_v - 2a_u a_w b_v b_w, \quad (30)$$

$$\tilde{D}_2 = -c_w^2 x_0 y_0 + b_v b_w x_0 + (a_u a_w + b_u b_w)y_0 - b_u b_v, \quad (31)$$

$$E_1 = -2a_u a_w b_u b_v + 2a_u^2 b_v b_w, \quad (32)$$

$$\tilde{E}_2 = -b_v b_w x_0^2 + (a_u a_w + b_u b_w)x_0 y_0 + b_u b_v x_0 - c_u^2 y_0, \quad (33)$$

$$F_1 = -a_w^2 b_u^2 + 2a_u a_w b_u b_w - a_u^2 b_w^2, \quad (34)$$

$$\tilde{F}_2 = \frac{c_w^2}{2}x_0^2 - (a_u a_w + b_u b_w)x_0 + \frac{c_u^2}{2}, \quad (35)$$

where $c_u^2 = a_u^2 + b_u^2$ and $c_w^2 = a_w^2 + b_w^2$.

The quadratic form can be described by five canonical parameters, as explained in Section 2.2: its center $(x_{00}, y_{00})^T$, its radii r_x and r_y, and its rotation angle β. The expression for the ellipse's center has already been given in main text, as well as its relationship with the projected center (cf. Eqs. (6) and (7)). The radii value:

$$r_{x,y} = -\frac{\sqrt{2\Delta(ce^2 + fb^2 - dbe + (d^2 - 4cf)a)}}{d^2 - 4cf}, \quad (36)$$

with $\Delta = c + f \pm \sqrt{(c-f)^2 + d^2}$. Apart from Eq. (8), there is a relationship for the sum of their squares:

$$r_x^2 + r_y^2 = \frac{\tilde{r}^2}{(1-\tilde{r}^2\cos^2\theta)^2}[\cos^2\theta(1-\tilde{r}^2 + x_0^2 + y_0^2) + \Phi], \quad (37)$$

with $\Phi = 2\sin\theta(\sin\theta + x_0\cos\theta\cos\phi + y_0\cos\theta\sin\phi)$.

Finally, by deriving the parametric forms of canonical ellipse equation, namely, $x = x_{00} + r_x\cos\beta\cos\alpha - r_y\sin\beta\sin\alpha$ and $y = y_{00} + r_x\sin\beta\cos\alpha + r_y\cos\beta\sin\alpha$, as a function of the angle α to find the angles α_x and α_y that zero them, after some manipulations the following expressions for the axis-aligned bounding box's sizes for Eq. (15) are obtained:

$$L_x^{\text{BBOX}} = 2\left|r_x\cos\beta\cos\alpha_x - r_y\sin\beta\sin\alpha_x\right|, \quad (38)$$

$$L_y^{\text{BBOX}} = 2\left|r_x\sin\beta\cos\alpha_y + r_y\cos\beta\sin\alpha_y\right|, \quad (39)$$

where $\alpha_{x,y} = \arctan\left(\mp\,(r_x/r_y)^{\pm 1}\,\tan\beta\right)$.

References

Ahn, S. J., Kotowski, R., 1997. Geometric image measurement errors of circular object targets. Optical 3-D Measurement

Techniques IV, 463–471.

Brown, D., 1971. Close-Range Camera Calibration. *Photogrammetric Engineering*, XXXVII(8), 855-866.

Canny, J., 1986. A computational approach to edge detection. *IEEE Transactions on pattern analysis and machine intelligence*, 679–698.

Dauvin, L., Drass, H., Vanzi, L., Dünner, R., Torres, M., Béchet, C., Boettger, D., Rojas, F., Shen, T. C., 2018. Optimization of Temperature, Targets, and Illumination for High Precision Photogrammetric Measurements. *IEEE Sensors Journal*, 18, 1449-1456.

Filion, A., Joubair, A., Tahan, A. S., Bonev, I. A., 2018. Robot calibration using a portable photogrammetry system. *Robotics and Computer-Integrated Manufacturing*, 49, 77-87.

Fitzgibbon, A. W., Fisher, R. B., 1995. A buyer's guide to conic fitting. *Proceedings of the 5th British Machine Vision Conference, Birmingham*, 513–522.

Förstner, W., 1984. Quality assessment of object location and point transfer using digital image correlation techniques. *International Archives of Photogrammetry*, 25(III), 197-219.

Gharaaty, S., Shu, T., Joubair, A., Xie, W. F., Bonev, I. A., 2018. Online pose correction of an industrial robot using an optical coordinate measure machine system. *International Journal of Advanced Robotic Systems*, 15, 1-16.

Ghosal, S., Mehrotra, R., 1993. Orthogonal moment operators for subpixel edge detection. *Pattern Recognition*, 26(2), 295-306.

Kager, H., 1981. Bündeltriangulation mit indirekt beobachteten Kreiszentren. *Geowissenschaftliche Mitteilungen der Studienrichtung Vermessungswesen der TU Wien*, 19.

Lavecchia, F., Guerra, M. G., Galantucci, L. M., 2018. Performance verification of a photogrammetric scanning system for micro-parts using a three-dimensional artifact: adjustment and calibration. *International Journal of Advanced Manufacturing Technology*, 96, 4267-4279.

Leizea, I., Herrera, I., Puerto, P., 2023. Calibration Procedure of a Multi-Camera System: Process Uncertainty Budget. *Sensors*, 23(2).

Luhmann, T., 2014a. Eccentricity in images of circular and spherical targets and its impact on spatial intersection. *The Photogrammetric Record*, 29, 417-433.

Luhmann, T., 2014b. Eccentricity in Images of Circular and Spherical Targets and its Impact to 3D Object Reconstruction. *The International Archives of the Photogrammetry, Remote Sensing and Spatial Information Sciences*, XL-5, 363-370.

Luhmann, T., Robson, S., Kyle, S., Boehm, J., 2020. *Close-Range Photogrammetry and 3D Imaging*. De Gruyter, Berlin, Boston.

Mendikute, A., Yagüe-Fabra, J. A., Zatarain, M., Álvaro Bertelsen, Leizea, I., 2017. Self-Calibrated In-Process photogrammetry for large raw part measurement and alignment before machining. *Sensors*, 17.

Mordwinzew, W., Tietz, B., Boochs, F., Paulus, D., 2015. Relevance of ellipse eccentricity for camera calibration. *Proceedings of Society of Photo-Optical Instrumentation Engineers*, 9528, 116-125.

Otepka, J., Fraser, C., 2004. Accuracy enhancement of vision metrology through automatic target plane determination. *Proceedings of the ISPRS congress, Istanbul, Turkey, 12–23 July 2004, vol. XXXV, part B*, ISPRS - International Archives of the Photogrammetry, Remote Sensing and Spatial Information Sciences, 873–879.

Otsu, N., 1979. A Threshold Selection Method from Gray-Level Histograms. *IEEE Transactions on Systems, Man, and Cybernetics*, 9(1), 62-66.

Pearson, K., 1895. Notes on regression and inheritance in the case of two parents. *Proceedings of the Royal Society of London*, 58, 240–242.

Pottler, K., Lüpfert, E., Johnston, G. H., Shortis, M. R., 2005. Photogrammetry: A Powerful Tool for Geometric Analysis of Solar Concentrators and Their Components. *Journal of Solar Energy Engineering*, 127, 94-101.

Robson, S., MacDonald, L., Kyle, S., Boehm, J., Shortis, M., 2018. Optimised multi-camera systems for dimensional control in factory environments. *Proceedings of the Institution of Mechanical Engineers, Part B: Journal of Engineering Manufacture*, 232, 1707-1718.

Shortis, M. R., Snow, W. L., Goad, W. K., 1995. Comparative geometric tests of industrial and scientific CCD cameras using plumb line and test range calibrations. *International Archives of the Photogrammetry, Remote Sensing and Spatial Information Sciences*, 30, 53-59.

Sims-Waterhouse, D., Isa, M., Piano, S., Leach, R., 2020. Uncertainty model for a traceable stereo-photogrammetry system. *Precision Engineering*, 63, 1-9.

Spearman, C., 1904. The Proof and Measurement of Association between Two Things. *The American Journal of Psychology*, 15(1), 72–101.

Suzuki, S., Abe, K., 1985. Topological structural analysis of digitized binary images by border following. *Computer Vision, Graphics, and Image Processing*, 30(1), 32-46.

Trinder, J., 1989. Precision of digital target location. *Photogrammetric Engineering Remote Sensing*, 55, 883-886.

Trujillo-Pino, A., Krissian, K., Alemán-Flores, M., Santana-Cedrés, D., 2013. Accurate subpixel edge location based on partial area effect. *Image and Vision Computing*, 31(1), 72-90.

Wang, J., Chen, J. et al., 2022. Subpixel edge detection algorithm based on improved Gaussian fitting and Canny operator. *Academic Journal of Computing & Information Science*, 5(7), 33–39.

Wrobel, B. P., 2012. Kreismarken in perspektiver Abbildung – im Bild und im Bündelblock. *Photogrammetrie Fernerkundung Geoinformation*, 3, 221-236.

Zakeri, E., Xie, W. F., 2024. Robust Photogrammetry Sensor-Based Real-Time Pose Control of Industrial Robots. *IEEE/ASME Transactions on Mechatronics*.